Powder Technology 305 (2017) 794–808

Contents lists available at ScienceDirect

Powder Technology

journal homepage: www.elsevier.com/locate/powtec

Experimentally validated numerical study of gas-solid vortex unit hydrodynamics

K. Niyogi, Maria M. Torregrosa, Maria N. Pantzali, Geraldine J. Heynderickx *, Guy B. Marin

Ghent University, Laboratory for Chemical Technology, Technologiepark 914, B-9052 Gent, Belgium

ARTICLE INFO

Article history:
Received 15 April 2016
Received in revised form 30 August 2016
Accepted 26 October 2016
Available online 29 October 2016

Keywords:
Gas-solid vortex unit
Rotating fluidized bed
Computational fluid dynamics
Eulerian multiphase modeling

ABSTRACT

A three-dimensional numerical analysis of the flow in a Gas-Solid Vortex Unit (GSVU) is carried out. The numerical model is first validated by comparing the bed pressure drop and solids velocity with experimental data. Next, the influence of gas flow rate, solids density, and particle diameter on the pressure drop, solids velocity, bed void fraction and slip velocity between the two phases is studied. A stable, solids bed is achieved for the entire range of gas flow rates tested (0.1–0.6 Nm^3/s). No particle entrainment is observed when varying the solid density (1800–450 kg/m^3) or the particle diameter (2–0.5 mm). A shift to bubbling fluidization regime is observed for small particle diameters (0.5 mm). The observed changes in the GSVU flow patterns are discussed by analyzing the changes in the cumulative centrifugal to drag force ratio over the bed.

© 2016 The Authors. Published by Elsevier B.V. This is an open access article under the CC BY-NC-ND license (http://creativecommons.org/licenses/by-nc-nd/4.0/).

1. Introduction

Gas-solid Fluidized Beds (FBs) are widely used in chemical industry as they enhance heat and mass transfer and solids mixing. The applications range from physical operations such as drying of solids [1], adsorption of dilute components from carrier gas [2] and particle coating [3] to reactive operations such as fluid catalytic cracking of hydrocarbons [4] and polymerization of olefins [5]. Heat and mass transfer efficiency in FBs is determined by the relative velocity between both phases, the so-called slip velocity. In conventional gravitational FBs, where the drag force is balanced by the gravitational force, the slip velocity cannot exceed the terminal free-falling velocity of the particles in a uniform bed operation [6]. Higher gas velocities in gravitational beds results in the formation of bubbles and slugs. Extensive gas bypass decreases gas-solid contact and thus the corresponding heat and mass transfer drops. Further increase in gas flow rate causes particle entrainment [7] and may affect the compactness of the industrial-scale fluidization setups [8].

Centrifugal force can reach much higher values than the gravitational force allowing feasible operation in the 7–40 g regime, which is suitable for high gas throughput, more uniform fluidization, higher slip velocities and, hence, much higher heat and mass transfer [9–13]. Centrifugal FBs cause a shift in the Geldart classification of particles [14] and have been successfully used in fluidization of cohesive particles [15,16]. Consequently the centrifugal bed technology is more energy efficient, increasing the gas flow rate per reactor volume and making the fluidization process more compact. Hence, a centrifugally fluidized bed is an ideal candidate for Process Intensification (PI).

A centrifugal FB can be achieved in two ways: by setting the particles in motion by rotating the operating vessel itself, known as Rotating Fluidized Bed (RFB) [13,17,18] or by introducing the particles in a swirling flow field of azimuthally injected gas in a static vessel (Gas-Solid Vortex Unit) (GSVU) [10,19–21]. In the RFB, the independent control over the rotational velocity of the vessel and the injected gas flow rate imply that the azimuthal and radial velocity components can be varied in a decoupled manner [13]. However, RFBs involve mechanically moving parts and are prone to mechanical abrasion. In GSVU's on the other hand, the fluidizing gas is injected from a number of azimuthally inclined rectangular slots at the circumferential wall. Azimuthal momentum is transferred from the swirling gas to particles fed into the unit, which start rotating and experience an outward centrifugal force. The particles rotating in a GSVR achieve a 'fluidized state' when the radially inward drag force exerted by the gas overcomes the apparent weight of solids in the centrifugal field [22]. Unlike the RFB, in the GSVU the particle velocity components cannot be independently controlled. However, the absence of mechanically moving parts significantly reduces the abrasion in the GSVU and makes the device more suitable for scale-up [19,23].

As the centrifugal force in a GSVU is a function of reactor geometry, operating conditions and solids properties, it can be tailored to establish a desired fluidization regime [17]. The latter cannot be achieved in gravitational FBs, as gravitational force is constant. All these features make the GSVU a potential device for PI of selected processes such as combustion of hydrocarbon fuels [24,25], drying of fine pored materials like food grains, pharmaceutical products or polymers [26,27], biomass pyrolysis [28] and SO_2-NO_x adsorption [29]. Excellent reviews of GSVU

* Corresponding author.
E-mail address: Geraldine.heynderickx@ugent.be (G.J. Heynderickx).

http://dx.doi.org/10.1016/j.powtec.2016.10.049
0032-5910/© 2016 The Authors. Published by Elsevier B.V. This is an open access article under the CC BY-NC-ND license (http://creativecommons.org/licenses/by-nc-nd/4.0/).

Nomenclature

A_P	cross-sectional area of a particle (m^2)
d_p	particle diameter (m)
e	dissipation of turbulent kinetic energy (m^2/s^3)
e_{ss}	restitution coefficient
F_c	cumulative centrifugal force over bed (N)
F_d	cumulative radial drag force over bed (N)
G_M	gas flow rate (Nm^3/s)
g	acceleration due to gravity (m/s^2)
k	turbulent kinetic energy (m^2/s^2)
L	GSVU length (m)
P	static pressure (Pa)
P_{gauge}	static gauge pressure (Pa)
ΔP_{bed}	bed pressure drop (Pa)
r	radial coordinate (m)
Re	Reynolds number
U	velocity (m/s)
U_{slip}	slip velocity (m/s)
V_P	volume of a particle (m^3)
V_T	total volume of particles (m^3)
z	axial position (m)
Greek letters.	
β	gas-solid drag coefficient (kg/m^3 s)
δ	angle of internal friction
ε	volume fraction
$\varepsilon_{s,max}$	maximum packing limit solids volume fraction
γ	dissipation of granular temperature by collisions ($kg/m\ s^3$)
λ_s	solids bulk viscosity (Pa s)
μ	granular viscosity (Pa s)
μ_{col}	solids collisional viscosity (Pa s)
μ_{fr}	solids frictional viscosity (Pa s)
μ_{kin}	solids kinetic viscosity (Pa s)
φ	specularity coefficient
Θ	granular temperature (J/kg)
ρ	phase density (kg/m^3)
θ	angular coordinate (rad)
τ	wall shear stress (N/m^2)
Subscripts.	
g	gas phase
s	solids phase
t	turbulent
col	collisional
fr	frictional
kin	kinetic
c	circumferential wall
e	end-wall

design as well as potential applications of single phase and multiphase vortex devices reference can be found in literature [16,30].

Reports on experimental studies carried out in GSVU setups to investigate the cold gas–solid hydrodynamics, i.e. in the absence of reactions, have improved the understanding of the nature of the flow field in the unit [11,12,19,31,32]. Kochetov et al. [33] ran experiments with varying length-to-diameter ratios of the GSVU and prescribed optimal values for its construction. Anderson et al. [19] performed experiments on GSVU bed hydrodynamics with talc, tungsten and zinc particles using X-ray absorption techniques to measure solids volume fractions in the bed and using a paddle wheel to measure angular bed velocities at various radii. Heat and mass transfer intensification when drying wheat grains in a GSVU was demonstrated by Volchkov et al. [34]. Particle entrainment close to the end-walls of the GSVU was observed as gas and solids centrifugal acceleration decrease in the wall boundary layers. Their work thus demonstrated the need for a 3D description of the GSVU bed hydrodynamics. Volchkov et al. [12] studied changes in the GSVU bed porosity behavior in the GSVU with varying gas flow rate and concluded that the bed becomes more dense with increasing gas flow rate. The authors also found the centrifugal force to be larger than the radial drag force in the GSVU under given flow conditions, indicating that, if centrifugal force and drag force do not balance each other, particles are pushed towards the wall resulting in increased wall shear stresses. De Wilde and de Broqueville [10,11] experimentally demonstrated by fast digital camera image analysis that the GSVU shows different fluidization behavior for different Geldart classified materials. Kovacevic et al. [31,32] used Particle Image Velocimetry (PIV) and pressure probing techniques to measure the pressure drop and solids velocity in a cold flow GSVU. The authors observed higher solids velocities with increasing gas flow rate and decreasing solids density. Depending on the solids loading, the GSVU bed exhibited bubbling characteristics for smaller sized particles.

Although the experimental work carried out by different researchers highlighted important GSVU flow characteristics, two major drawbacks of the experimental data acquisition remain. Firstly, the range of operating conditions is limited by equipment design. More importantly, the non-intrusive measurements techniques employed limit experimental data collection to locations near the end-walls due to the dense nature of the bed [32]. However, for a complete description of the GSVU bed hydrodynamics various interactions at multiple scales (viz. at particle scale, bubble/slug scale and reactor scale) need to be accounted for [34–36]. The lack of complete information on the internal bed hydrodynamics of centrifugal FBs necessitates the need for a numerical study [13]. de Broqueville and De Wilde [37] performed two-dimensional (2D) numerical heat transfer studies in a GSVU. The authors theoretically demonstrated an increased heat transfer thereby achieving a more uniform heat distribution and a higher bed-averaged heat transfer rate compared to the conventional gravitational bed riser. Rosales and De Wilde [36] captured the appearance of slugs and non-uniformities in the bed for small sized catalyst particles (80 μm) in a 2D numerical study. Ashcraft et al. [28] implemented 2D simulations for biomass pyrolysis and demonstrated PI in a GSVU. These numerical studies although highly insightful, are 2D in nature and cannot capture the effect of a unidirectional gas exhaust or the presence of the end-walls on bed hydrodynamics. Moreover, bubble formation and slugging in fluidized beds may possess 3D propagation tendencies [38]. Hence, in order to properly investigate the bed (non-)uniformity in the GSVU, 3D simulations are needed. Preliminary 3D simulations using various geometrical designs of the GSVU have been carried out by Dutta et al. [23]. However, elaborate studies on the effect of gas flow rates and different solids properties were not performed. Furthermore, the validation of the applied CFD model was purely qualitative, requiring further calibration of the numerical model.

In the present work, the commercial Computational Fluid Dynamics (CFD) code FLUENT® 14.0 is used to perform a three-dimensional (3D) numerical study of the hydrodynamic behavior of the GSVU. First, the CFD model is validated by comparing simulated pressure and velocity data with experimental data. Next, the validated numerical model is used to study the gas-solid hydrodynamics in the GSVU over a wide range of conditions. Gas flow rate, particle diameter and solids density are individually varied to estimate their effect on various flow variables such as pressure drop, solids velocity, bed-averaged solids volume fraction and slip velocity.

2. Methodology

2.1. GSVU setup

A photographic view of the experimental GSVU setup, simulated in this work, is shown in Fig. 1(a). A schematic of the setup, shown in

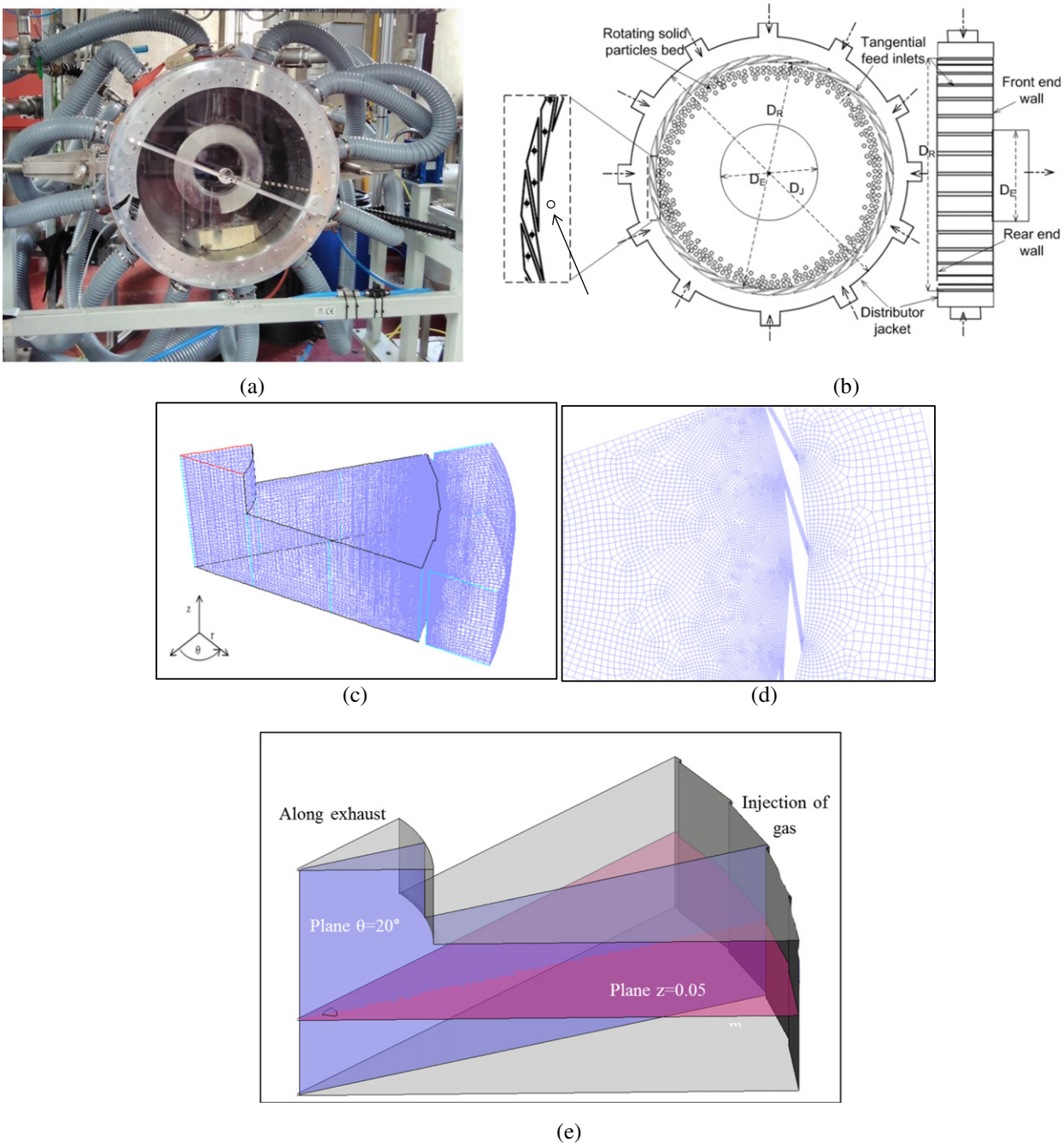

Fig. 1. (a) Photographic view of the Gas-Solid Vortex Unit; (b) front view and side view of the pilot-scale GSVU [39]; (c) 3D periodic mesh used to simulate GSVU hydrodynamics; (d) zoomed-in view of mesh refinement near slots and (e) different analysis planes in the sectional GVU simulation geometry. Geometrical dimensions given in Table 1.

Fig. 1(b) [39], clearly highlights the important sections of the geometry. It basically consists of a cylindrical unit positioned along a horizontal axis with thirty-six gas injection slots azimuthally inclined at a 10° angle, equally distributed over the circumferential wall. The unit is confined on two sides by two parallel flat end-walls made from transparent polycarbonate glass (Makrolon®), allowing visual inspection of the solids bed formed in the GSVU as well as PIV measurements. The distance in between the end-walls determines the length of the GSVU. On the front end-wall (see Fig. 1(b)) a unidirectional gas exhaust is present. The fluidizing gas is first sent to an outer concentric distributor jacket through 12 feeding pipes positioned normally with respect to the jacket wall. The distribution jacket ensures that the gas approaching each injection slot has a nearly similar velocity. For a given gas flow rate, the thickness of the injection slots determines the magnitude of the gas injection velocity while the injection angle determines its radial and azimuthal components. For instance, in the given GSVU geometry with thirty-six 2 mm injection slots, a gas flow rate of 0.5 Nm^3/s approximately corresponds to 70 m/s average injection velocity magnitude at the slots. The 10° injection angle of the azimuthally inclined slots then

Table 1
Geometrical data for the pilot-scale experimental GSVU.

GSVU circumferential wall diameter	0.54 m
GSVU exhaust diameter	0.15 m
GSVU length	0.1 m
Number of injection slots	36
Slot thickness	0.002 m
Slot angle with respect to circumferential wall	10°

results in approximately 68 m/s average azimuthal gas injection velocity and 12 m/s average radial gas injection velocity at the slot opening. Table 1 lists up the main dimensions of the GSVU. The GSVU is operated in semi-batch mode. At the start of the experiment, the fluidizing gas is fed to the unit until a steady-state swirling gas flow is established inside the chamber. A more detailed description of the experimental setup and experimental procedure can be found in previous Kovacevic et al. [31, 32]. Some details of the experimental procedure, relevant for the numerical study of the GSVU are discussed next.

Pressure measurements are carried out using radially aligned pressure taps on the rear end-wall of the unit, with milliampere output pressure sensors (Unik 5000). A two-dimensional standard PIV system from LaVision® with a 4 MP Charge Couple Device Camera and a 135 mJ Nd-YAG laser are used to measure the solids velocity through the transparent rear end-wall of the unit. A more detailed description of the measurement techniques can be found in Kovacevic et al. [31] and Pantzali et al. [40]. The pressure and velocity measurements performed for different operating conditions and particle properties are used to validate the CFD model proposed for the numerical study of the GSVU.

2.2. Numerical model

In the present numerical study the Eulerian-Eulerian approach [41] is adopted to simulate the two-phase flow, using the commercial CFD software package Fluent 14.a®. In this approach, the gas and solid phases are treated as interpenetrating continua. Table 2 summarizes the conservation equations for both phases. The mass and momentum conservation equations are Reynolds-averaged. For the solid phase, the conservation equations for mass, momentum and granular temperature are obtained via the Kinetic Theory of Granular Flow (KTGF) [42, 43]. The effect of turbulence is taken into account for each phase via a Re-Normalization Group (RNG) k-ε model [44], adapted for gas-solid interactions. No energy conservation equations are applied since isothermal operation is assumed for both phases in the present study.

Simulating the whole GSVU geometry is computationally expensive. Ashcraft et al. [28] confirmed that simulating a 40° section of the GSVU, using rotational periodic boundary conditions, suffices to obtain correct values for primary flow variables such as pressure drop, solids volume fraction and solids velocity. Hence, 3D simulations of a 40° section of the unit are performed. The 3D simulations help to capture the effect of the end-walls on the gas-solid flow behavior and to make the simulation results accurate. Initially a mesh study is performed to verify the grid independence of the presented simulation data. Three mesh resolutions (I, II and III) are used (Table 4). The consecutive mesh size is decreased by a factor of 2. In Table 4 the change in the calculated values for the time-averaged GSVU pressure drop, solids velocity magnitude and solids volume fractions are presented. The difference in flow variable values between mesh II and III is found to be small (<5%) and hence, mesh II (shown in Fig. 1(c)–(d)) is chosen as the standard mesh for further analysis in order to save computational cost. The cell size in the mesh varies from 0.5 mm near the gas injection slots to 4.0 mm near the central gas exhaust. Cell sizes are smaller near the circumferential wall to capture the small time- and space-scale hydrodynamics near the solids bed [31]. The cells close to the end-walls of the GVU are more densely packed to give a grid resolution with wall y^+ values in the order of 30. The standard wall function model proposed by Launder and Spalding [45] is used to model the near-wall flow. Remark that simulation of a sectional GSVU geometry with horizontal axis implies that the gravitational force cannot be accounted for correctly as the gravitational acceleration direction changes in different sections of the geometry. Gravity was shown to have a minimal effect on the flow dynamics at the applied operating conditions [31]. During simulations only the dominant forces, that is centrifugal force, drag force, inter-particle and particle-wall forces, are taken into consideration.

An overview of the constitutive equations is found in Table 3. The gas is considered to be incompressible (air, density: 1.225 kg/m^3) and the no-slip boundary condition is imposed at both end-walls and circumferential wall for the gas phase. In order to reduce the computational cost, the exhaust tube is simulated over a length of 0.1 m only. The radial

Table 3
Constitutive equations.

$$\overline{\overline{\tau_g}} = \varepsilon_g(\mu_g + \mu_{t,g})(\nabla \overline{U_g} + \nabla \overline{U_g}^T) \quad (3.1)$$

Granular Temperature: [42]

$$(-P_s\bar{\bar{I}} + \overline{\overline{\tau_s}}) : \nabla \overline{U_s} - \gamma\Theta_s + 3\beta\Theta_s = 0 \quad (3.2)$$

Solids pressure [54]:

$$P_s = \rho_p\varepsilon_s\theta + 2(1+e_{ss})\rho_p\theta g_{0,ss}(\varepsilon_s)\varepsilon_s^2 \quad (3.3)$$

Gas-solid drag coefficient [53]:

$$\beta = \tfrac{3}{4}C_D\frac{\varepsilon_g\varepsilon_s\rho_g|\overline{U_{slip}}|}{d_p}\varepsilon_g^{-2.65}(\text{for } \varepsilon_g > 0.8)$$
$$\text{where } C_D = 150\frac{24}{\varepsilon_g \mathrm{Re}_s}[1 + 0.15(\varepsilon_g \mathrm{Re}_s)^{0.687}];\ \mathrm{Re}_s = \frac{\rho_g d_p|\overline{U_{slip}}|}{\mu_g} \quad (3.4)$$
$$\beta = 150\frac{\varepsilon_s^2\mu_g}{\varepsilon_g d_p^2} + 1.75\frac{\rho_g\varepsilon_s|\overline{U_{slip}}|}{d_p}(\text{for } \varepsilon_g \le 0.8)$$

Radial distribution function [55]:

$$g_{0,ss} = \left[1 - \left(\frac{\varepsilon_s}{\varepsilon_{s,\max}}\right)^{\frac{1}{3}}\right]^{-1} \quad (3.5)$$

Solid-phase shear stress tensor:

$$\overline{\overline{\tau_s}} = \varepsilon_s\mu_s(\nabla \overline{U_s} + \nabla \overline{U_s}^T) + \varepsilon_s(\lambda_s - \tfrac{2}{3}(\mu_{s,col} + \mu_{s,kin} + \mu_{s,fr} + \mu_{t,s}))\nabla \cdot \overline{U_s}\,\bar{\bar{I}} \quad (3.6)$$

Solids collision viscosity [53]:

$$\mu_{s,col} = \tfrac{4}{5}\varepsilon_s\rho_s d_p g_{0,ss}(1 + e_{ss})\left(\tfrac{\Theta_s}{\pi}\right)^{1/2} \quad (3.7)$$

Solids kinetic viscosity [56]:

$$\mu_{s,kin} = \frac{\varepsilon_s\rho_s d_p\sqrt{\Theta_s\pi}}{6(3-e_{ss})}[1 + \tfrac{2}{5}\varepsilon_s g_{0,ss}(1 + e_{ss})(3e_{ss} - 1)] \quad (3.8)$$

Solids frictional viscosity [57]:

$$\mu_{s,fr} = \frac{P_s \cdot \sin\hat{\phi}}{2\sqrt{I}} \quad (3.9)$$

Solids bulk viscosity [54]:

$$\lambda_s = \tfrac{4}{3}\varepsilon_s\rho_s d_p g_{0,ss}(1 + e_{ss})\left(\tfrac{\Theta_s}{\pi}\right)^{1/2} \quad (3.10)$$

Shear stress at the wall [49]:

$$\overline{\overline{\tau}}_s = -\tfrac{\pi}{6}\sqrt{3}\varphi\frac{\alpha_s}{\alpha_{s,\max}}\rho_s g_{0,ss}\sqrt{\Theta_s}|\overline{U_{slip}}| \quad (3.11)$$

where φ is the specularity coefficient

Table 2
Conservation equations.

Mass Conservation:

$$\frac{\partial}{\partial t}(\varepsilon_i\rho_i) + \nabla \cdot (\varepsilon_i\rho_i\overline{U_i}) = 0 (\mathrm{i} = \mathrm{g}, \mathrm{s}) \quad (2.1)$$

Gas Momentum Conservation:

$$\frac{\partial}{\partial t}(\varepsilon_g\rho_g\overline{U_g}) + \nabla \cdot (\varepsilon_g\rho_g\overline{U_g}\,\overline{U_g}) = -\varepsilon_g\nabla P + \nabla \cdot \overline{\overline{\tau_g}} + \varepsilon_g\rho_g\bar{g} - \beta(\overline{U_g} - \overline{U_s}) \quad (2.2)$$

Solids Momentum Conservation:

$$\frac{\partial}{\partial t}(\varepsilon_s\rho_s\overline{U_s}) + \nabla \cdot (\varepsilon_s\rho_s\overline{U_s}\,\overline{U_s}) = -\varepsilon_s\nabla P - \nabla P_s + \nabla \cdot \overline{\overline{\tau_s}} + \varepsilon_s\rho_s\bar{g} - \beta(\overline{U_s} - \overline{U_g}) \quad (2.3)$$

Transport equation for k, turbulent kinetic energy: (i = g, s)

$$\frac{\partial}{\partial t}(\varepsilon_i\rho_i k) + \nabla \cdot (\varepsilon_i\rho_i k\overline{U_i}) = \nabla \cdot (\varepsilon_i\frac{\mu_{t,i}}{\sigma_j}\nabla k) + (\varepsilon_i\mu_{t,i}(\nabla \overline{U_i} + \overline{U_i}^T) : \nabla \overline{U_i} - \varepsilon_i\rho_i e) - \beta(2k) \quad (2.4)$$

Transport equation for e, dissipation rate of turbulent kinetic energy: (i = g, s)

$$\frac{\partial}{\partial t}(\varepsilon_i\rho_i k) + \nabla \cdot (\varepsilon_i\rho_i k\overline{U_i}) = \nabla \cdot (\varepsilon_i\frac{\mu_{t,i}}{\sigma_j}\nabla k) + (\varepsilon_i\mu_{t,i}(\nabla \overline{U_i} + \overline{U_i}^T) : \nabla \overline{U_i} - \varepsilon_i\rho_i e) - \beta(2k) \quad (2.5)$$
$$c$$

The turbulent viscosity $\mu_{t,i}$ in equations (2.3-2.4) can then be computed from: (i = g, s)

$$\mu_{t,i} = \rho_i C_\mu\frac{k^2}{e} \quad (2.6)$$

Table 4
Mesh study for the GSVU simulations.

Mesh	Number of cells	Simulated variable values		
		ΔP_{gauge} (kPa)	$U_{\theta,s}$ (m/s)	ε_s (−)
I	124,420	3.1	6.1	0.44
II	256,000	4.2	7.84	0.49
III	557,330	4.4	7.92	0.51

Table 5
Optimized CFD model parameters.

Parameter	Value
Particle end-wall specularity coefficient (φ_e)	0.004
Particle circumferential-wall specularity coefficient (φ_c)	0.02
Particle restitution coefficient (e_{ss})	0.9
Maximum packing limit	0.63
Turbulent intensity at injection slots/exhaust	5%

equilibrium pressure distribution condition is imposed at the exhaust outlet as previous studies have shown that the outflowing gas still retains its swirling structure at this height [46]. Experimental observations have shown that the solids bed formed in the GSVU is dense in nature [23,32]. Particle collisions are modeled as highly elastic imposing a restitution coefficient (e_{ss}) value of 0.9. Remark that the collision dynamics between two polymeric particles primarily depends on impact velocity [47,48]. The cold flow experimental GSVU studies have been performed with materials such as high density polyethylene (HDPE), a semi-crystalline material and polycarbonate (PC), a more amorphous material. However, both materials exhibit a similar elastic collision tendency with a restitution coefficient close to 0.9 for low impact velocities (<1 m/s) [47]. The solids bed formed in the GSVU is shown to be dense, with layers of solids rotating in very close proximity to each other near the circumferential wall of the unit [32]. For dense flow, direct inter-particle collisions at velocities higher than 1 m/s are less likely. The inter-particle momentum transfer primarily takes place through shear. Consequently the frictional forces between the particle layers become important rather than collisional dynamics. The partial-slip wall boundary condition developed by Johnson and Jackson [49] is used to calculate the solid shear stress near the wall. The specularity coefficient used differs for the circumferential wall ($\varphi_c = 0.02$) and the end-walls ($\varphi_e = 0.004$). Different wall construction materials (circumferential wall: steel, end-wall: polycarbonate glass, Makrolon®) explain the need for different values of specularity coefficients. All CFD model parameters are presented in Table 5. The turbulent intensity is set at a value of 5% at the jacket outer periphery (r = 0.35 m). The high value artificially replicates the high turbulence due to the sudden expansion of the fluidizing gas entering the jacket through discrete feeder pipes in (r = 0.35 m) the experimental setup. The possibility of flow reversal near the exhaust of the unit due to vortex breakdown may result in increased turbulence at the exhaust, explaining the high turbulent intensity value imposed at the exhaust. Remark that, with both the jacket wall and the central gas exhaust being sufficiently away from the solids bed region in the GSVU, the turbulence boundary conditions will only have a minor influence on the overall time-averaged solids bed hydrodynamics. The conditions for the complete numerical study, comprising of 12 simulation cases, are presented in Table 6. The experimentally measured and computationally determined gauge pressures and azimuthal solids velocities for different gas flow rates, particle diameters and solid densities (corresponding to simulation cases 3, 4, 10 in Table 6) are compared in Fig. 2(a)–(e). The gauge pressure data from simulations and experiments compare well in the disc part of the GSVU (0.06 < r < 0.27 m), as seen in Fig. 2(a)–(b). The average percentage deviation between the experimental and simulated pressure data is around 5% in the main disc part of the GSVU. It significantly increases near the core of the exhaust region (r < 0.06 m). The latter can be attributed to the shortening of the simulated exhaust line as compared to the experimental setup to reduce computational cost. As the main focus of the manuscript is on the solids bed hydrodynamics in the disc part of the unit, differences near the exhaust do not exert any significant influence on the results discussed in the presented study. The experimental and simulated solids velocities are compared in Fig. 2(c)–(e). With an average percentage deviation of 7%, the data sets agree well for the main part of the solids bed. The deviation increases towards the free board of the solids bed and in the vicinity of the circumferential wall (~20%). In these particular regions the differences can be attributed to the inability of the experimental technique to provide mass-averaged velocity values, as calculated from simulations. The PIV technique indeed cannot account for local solids volume fractions in the solids bed. The difference between the experimental and simulated data close to the circumferential wall stems from a calculated narrow region of dilute solids flow close to the circumferential wall of the unit. As mass-averaged solids velocities are calculated in the simulations, the solids velocities near the circumferential wall of the GSVU are low. The PIV technique only provides absolute velocities of particle clusters without accounting for the fact that lesser number of particles near the circumferential wall will result in a decrease in the local solids volume fractions. Also, the geometrical design of the GSVU makes it difficult to accurately measure local solids volume fractions at such close distance to the circumferential wall. Hence, the main objective of the presented study is the analysis of the overall GSVU solids bed characteristics. Difference of local velocity data close to the circumferential wall between experiments and simulations lies within acceptable limit. The pressure and velocity data presented in Fig. 2(a)–(e) validates the CFD model for further numerical study of the GSVU hydrodynamics. After validating the numerical model, a parametric study under varying conditions of gas flow rate and particle properties is carried out to obtain a better understanding of the gas-solid hydrodynamic behavior in the GSVU. The effect of one parameter on the hydrodynamic performance of the GSVU is studied in detail, meanwhile keeping the others constant.

2.3. Solution method

To solve the set of equations the segregated pressure-based Phase Coupled SIMPLE (PC-SIMPLE) algorithm [50] is used. A second-order implicit time stepping scheme is applied for the transient simulations. Reaching the steady-state semi-batch fluidized bed condition is a two-step process. The first step involves establishing a steady-state gas-only flow inside the GSVU (previously described as the start of an experiment). Once the steady-state swirling gas flow is reached (about 5 s simulation time), the particles are fed with the gas through the injection slots until a stable solids bed is established. Remark that this feeding mechanism differs from the experimental one. However, the focus of the present study is on the analysis of steady-state semi-batch hydrodynamics in the GSVU, the simulation results will not be affected by the procedure through which the particles are fed into the geometry. In the semi-batch mode, particles are fed until a designated mass of solids has accumulated in the unit (2 kg in the presented cases). Next, solids feeding is stopped. Experimental data on solids bed hydrodynamics is collected when sufficient time has elapsed to reach steady-state operation. In the simulations, solids feeding is monitored by tracking the solids accumulation in the main unit. When the designated bed mass is reached and steady state solids flow is achieved, time-averaging of flow characteristics is performed. The semi-batch operation of the GSVU thus ensures that the hydrodynamic data from experiments and simulations are not influenced by the solids feeding mechanism. Feeding is stopped once the required bed mass is obtained (about 2 s simulation time). Once the gas-solid flow has reached steady-state, another 10 s of simulation time is required for the time-averaging of the bed hydrodynamics. The time step during the transient simulations varies from an initial 10^{-3} s during gas and solids feeding, to 10^{-2} s as stable bed operation approaches. Each time step takes 50 iterations. The simulations are

Table 6
Simulation cases for parametric study.

		Gas flow rate (G_M) Nm^3/s	Particle diameter (d_p) mm	Particle density (ρ_s) kg/m^3
Effect of gas flow rate	Case 1	0.11	1	950
	Case 2	0.23		
	Case 3	0.32		
	Case 4	0.41		
	Case 5	0.52		
	Case 6	0.64		
Effect of particle density	Case 7	0.32	1	450
	Case 8			950
	Case 9			1800
Effect of particle diameter	Case 10	0.32	2	950
	Case 11		1	
	Case 12		0.5	

performed on AMD-based Linux 32-core clusters. A 3D time-averaged steady-state solution for a 40° sectional volume of the GSVU requires about 2 weeks of CPU time. The time-averaged data are exported for post-processing and further analysis. A normal-to-axis z = 0.05 m plane and an θ = 20° azimuthal plane are selected for analysis of the simulation results. They are indicated as colored planes in Fig. 1(e).

3. Results and discussion

3.1. Particle-free GSVU hydrodynamics

As previously mentioned, both GSVU experiments and simulations start by establishing a steady-state swirling gas flow inside the unit. Therefore, as an introduction to the two-phase study and for means of comparison with the particulate flow hydrodynamics, a short overview of particle-free GSVU hydrodynamics is provided. The results discussed in this section are obtained for a gas flow rate (G_M) of 0.39 Nm^3/s.

Fig. 3(a) shows the steady-state azimuthal gas velocity profile in the particle-free GSVU along the radial coordinate. From the circumferential wall to the gas exhaust (0.075 < r < 0.27 m) the azimuthal gas velocity increases with decreasing radial coordinate, a behavior representative of free-vortex flow dynamics. This free-vortex flow behavior in the disc part of the GSVU, predicted by the simulations, compare well with LDA velocity data from experiments by Volchkov et al. [12]. The azimuthally injected gas spirals its way, radially converging, towards the central gas exhaust forming a free-vortex flow region in the disc part

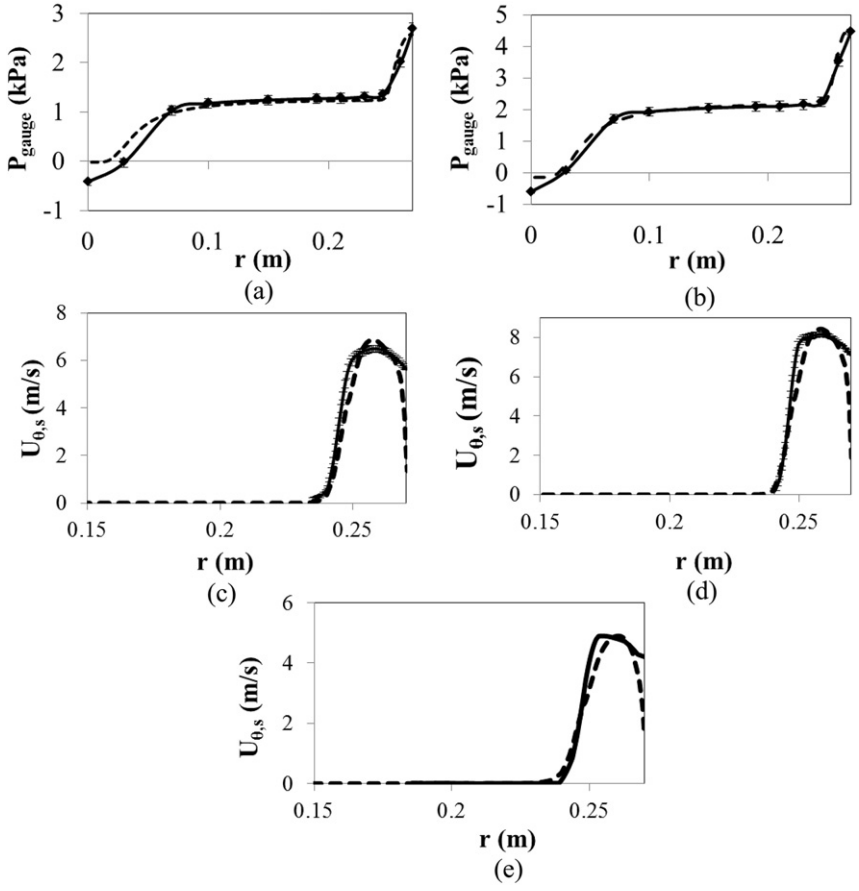

Fig. 2. Radial profiles of static gauge pressure for particulate flow along z = 0.05 m line in θ = 20° plane: full line, experimental data and (−) numerical data calculated by solving Eqs. (2.1)–(3.11) in Tables 2 and 3 with parameter values in Table 5, for (a) G_M = 0.39 Nm^3/s, d_p = 1 mm, ρ_s = 950 kg/m^3; (b) G_M = 0.5 Nm^3/s, d_p = 1 mm, ρ_s = 950 kg/m^3. Radial profiles of azimuthal solids velocity for particulate flow along the θ = 20° plane, z = 0.05 m line: full line, experimental data; (−) numerical simulation calculated by solving Eqs. (2.1)–(3.11) in Tables 2 and 3 with parameter values in Table 5, for (c) G_M = 0.39 Nm^3/s, d_p = 1 mm, ρ_s = 950 kg/m^3; (d) G_M = 0.5 Nm^3/s, d_p = 1 mm, ρ_s = 950 kg/m^3 and (e) G_M = 0.39 Nm^3/s, d_p = 2 mm, ρ_s = 950 kg/m^3. Bed mass = 2 kg. Error bars represent the 95% confidence interval based on three repeated experiments.

of the GSVU. Upon reaching the unidirectional central gas exhaust a strong positive axial velocity component develops and disrupts the swirling structure of the gas flow resulting in a drastic reduction of the azimuthal velocity.

Fig. 3(b) shows the steady-state static gauge pressure profile plotted along the radial coordinate for particle-free flow. The pressure drop over the unit is computed to be about 15 kPa. The free-vortex structure in the GSVU causes the azimuthal gas velocity component to dominate the axial and radial components by an order of magnitude, thus reducing the single-phase Navier-Stokes equation for the radial coordinate to the cyclostrophic balance [40]:

$$\frac{\partial P}{\partial r} = \frac{\rho U_{\theta,g}^2}{r} \tag{1}$$

The cyclostrophic balance indicates that the radial pressure gradient inside the GSVU in particle-free flow is balanced by the strong centrifugal acceleration of the gas. In other words, the high azimuthal velocity component of the free swirling gas causes the high pressure drop over the unit.

The negative static gauge pressure for $r < 0.05$ m indicates flow reversal in the central gas exhaust region of the GSVU ($0 < r < 0.05$ m). This flow reversal zone is referred to as the backflow region in the GSVU. As the swirling gas, approaching from the injection slots, reaches the central gas exhaust, it has to bend 90° towards the unidirectional exhaust. This high degree of streamline bending around the axis of the exhaust causes flow acceleration due to an abrupt change in velocity direction and creates a local low pressure region. A gas recirculation zone develops in the exhaust region in the GSVU, reducing the net exit area of the gas flowing through the exhaust tube. The gas leaves the GSVU only through an annular ring-like cross-section of the exhaust pipe. This decrease in the exhaust area increases the overall pressure drop over the unit.

3.2. Particulate GSVU hydrodynamics

3.2.1. Pressure drop and gas dynamics

Once steady-state gas flow has been established in the GSVU, particles with 1 mm diameter (d_p) and 950 kg/m^3 (ρ_s) solids density are fed until a bed mass of 2 kg is achieved. As more particles are fed into the GSVU, the "height" of the solids bed increases radially inwards. When sufficient particles are fed, a dense stable solids bed is formed near the circumferential wall. The present study focuses on stable bed hydrodynamics only. Bed stability is discussed in more detail by Kovacevic et al. [31].

As seen in Fig. 3(b), the total pressure drop over the GSVU is seen to decrease from 15 kPa in particle-free flow to 3 kPa in particulate flow. In gravitational fluidized beds, the presence of particles provides a physical barrier for the gas flow and the pressure drop increases as compared to particle-free flow. The pressure profiles for the GSVU show a reverse trend as can be seen in Fig. 3(b) and as experimentally observed [40, 51]. For particulate flow, the pressure drop is mainly localized over the solids bed (ΔP_{bed}). From the freeboard region to the central exhaust the pressure remains nearly constant. In the exhaust zone, a slight pressure drop is observed. Introduction of particles in the GSVU immediately disrupts the swirling structure of the gas in the particle-free GSVU. This can be observed in Fig. 3(a), where the azimuthal gas velocity is significantly reduced (around 80%) when the particles fed form a stable bed. The gas loses the major part of its azimuthal momentum by imparting rotational momentum to the particles. When the gas leaves the bed, the gas velocity is of the order of 5 m/s, that is one order of magnitude smaller than the values in particle-free flow (Fig. 3(a)). The reduced azimuthal gas velocity component fails to generate a strong swirling structure in the particle-free zone between the freeboard and the central gas exhaust ($0.075 < r < 0.24$ m). The weaker swirling structure results in a lower radial pressure drop, following the cyclostrophic balance (Eq. (1)). From Fig. 3(b) it can also be seen, that in the exhaust region ($0 < r < 0.075$ m) the negative gauge pressure values observed in particle-free flow becomes negligible when particles are introduced. This provides an indication that the presence of particles diminishes the backflow region around the exhaust axis (discussed in previous section). To further confirm this hypothesis, an in-plane gas velocity vector field in the $\theta = 20°$ plane in the GSVU for particle-free flow (Fig. 4(a)) and particulate flow (Fig. 4(b)) are compared. It can be clearly seen from the figure, that the backflow region is substantially reduced by the introduction of particles in the GSVU, increasing the net cross-sectional area for the gas to leave. Fig. 4(c), showing the axial gas velocity profiles with respect to the radial coordinate in the exhaust tube in the $\theta = 20°$ plane at $z = 0.12$ m, shows that the presence of particles reduces the radius of the backflow region (indicated by negative axial velocity values). The width of the annular region where the gas leaves from the unit increases from around 0.02 m (particle-free flow) to 0.05 m (particulate flow). Thus the cross-sectional area for the gas to leave the unit increases by a factor of 1.7. The axial gas velocities in the exhaust tube decrease accordingly. According to Bernoulli's law, a reduced gas velocity results in an increased local gauge pressure value. Consequently, the static gauge pressure drop in the exhaust region

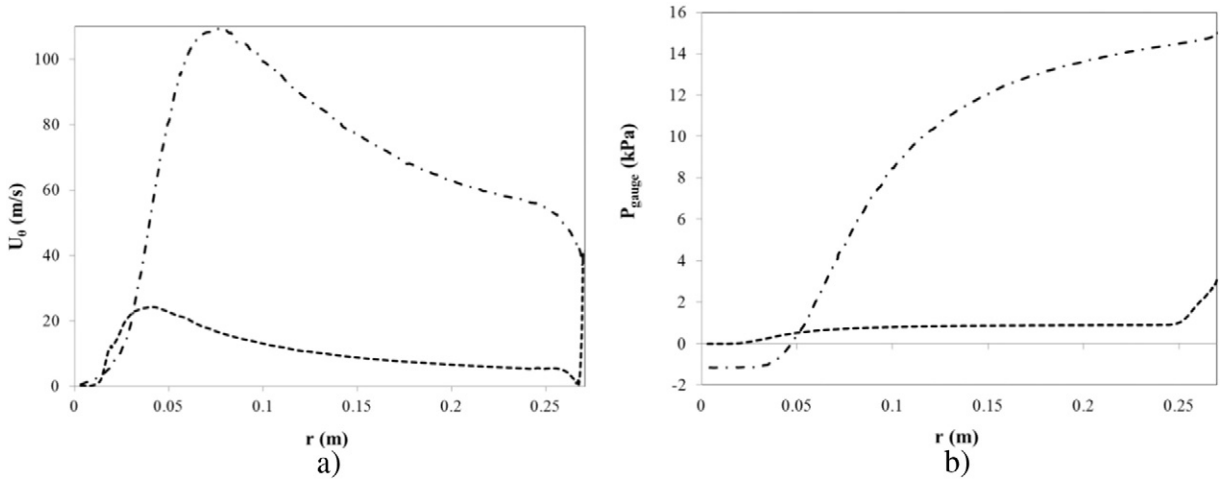

Fig. 3. (a) Radial profiles of (a) azimuthal gas velocity and (b) static gauge pressure along $z = 0.05$ m line in $\theta = 20°$ plane: (-●-) particle-free flow calculated by solving the set of Eqs. (2.1)–(2.2), (2.4)–(2.6) in Table 2, for $G_M = 0.39$ Nm^3/s and (—) particulate flow, calculated by solving the set of Eqs. (2.1)–(3.11) in Tables 2 and 3 with parameter values in Table 5, for $G_M = 0.39$ Nm^3/s, $d_p = 1$ mm, $\rho_s = 950$ kg/m^3. Bed mass = 2 kg.

decreases (Fig. 3(b)). The total decrease in pressure drop over the entire GSVU when introducing particles is thus explained both by the disruption of the swirling gas flow structure and by the size-reduction of the backflow region.

3.2.2. Solids volume fraction and velocity

The radial solids volume fraction distribution along the bed in the GSVU is presented in Fig. 5(a). The bed shows a dense middle part and becomes diluted towards the circumferential wall ($r = 0.27$ m) and towards the freeboard ($r < 0.25$ m). In the middle of the bed, solids volume fractions are close to 0.63, the maximum packing limit for spherical monodisperse particles [18]. A solids volume fraction of 0.05 is considered to be the cut-off value to locate the bed freeboard. From Fig. 5(a), it is seen that the bed height is about 0.03 m. An experimental value of bed height with value of 0.026 m was observed and previously reported [32]. The bed is calculated to be most dense at a radius of 0.255 m. At the circumferential wall the solids volume fraction is as low as 0.4 due to the injection of gas through the slots. The dense solids bed acts like a gas distributor, splitting the inflowing gas into multiple streams. A gas stream flowing close to the circumferential wall induces a decrease in the solids volume fraction in the proximity of the circumferential wall. To verify this hypothesis, the gas velocity vectors are plotted along with the solids volume fraction field in the $z = 0.05$ m plane in Fig. 5(b). It is indeed discerned that although most of the azimuthally entering gas flows radially inwards through the bed towards the central gas exhaust, a part of it flows azimuthally very close to the circumferential wall. The lowering of solids volume fractions predicted by the simulations compare qualitatively well with experimental X-ray absorption data obtained by Anderson et al. [19].

A profile of the azimuthal solids velocity along the radial coordinate was already plotted in Fig. 2(c), when comparing the simulated and experimental solids velocity data. Near the circumferential wall the azimuthal solids velocity is reduced due to particle-wall friction. The subsequent particle layers away from the wall accelerate and a maximum azimuthal solids velocity of about 7 m/s is obtained at $r = 0.255$ m where the bed is most dense ($\varepsilon_s = 0.61$) (Fig. 5(a)). Beyond this point, the azimuthal solids velocity gradually decreases. This can be attributed to shear between the particle layers on the one hand and reduced momentum transfer between the phases on the other. The reduction in azimuthal solids velocity near the freeboard was also experimentally observed by Kovacevic et al. [32].

3.2.3. Slip velocity between gas and solid phases

As the gas flows through the bed it exerts a drag force on the particles. The slip velocity between both phases, on particle scale, is a prime variable to determine the value of this drag force. Studying the GSVU hydrodynamics based on the balance between drag force and centrifugal force thus requires determination of proper slip velocity values. Since the gas-solid hydrodynamics in the GSVU is not purely

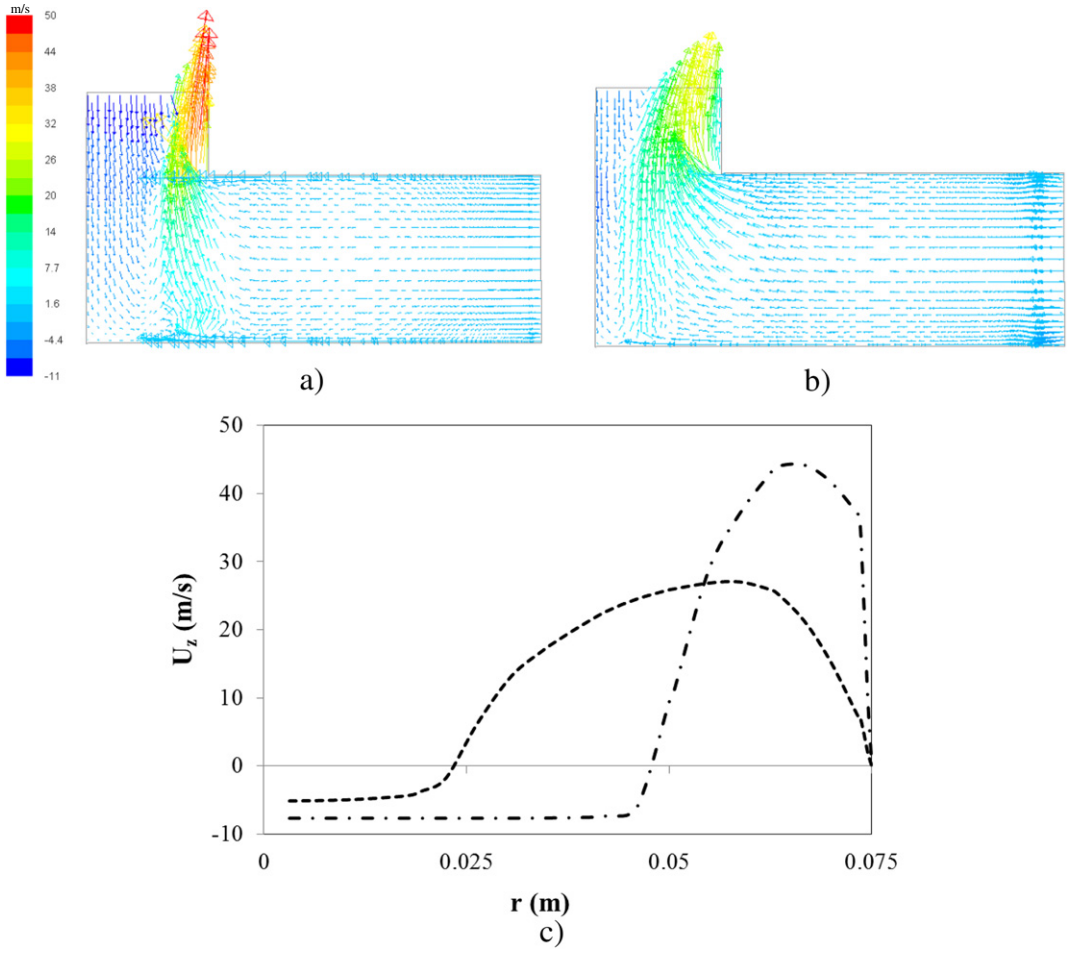

Fig. 4. Velocity vector field in $\theta = 20°$ plane for (a) particle-free flow calculated by solving the set of Eqs. (2.1)–(2.2), (2.4)–(2.6) in Table 2, for $G_M = 0.39$ Nm^3/s and (b) particulate flow calculated by solving Eqs. (2.1)–(3.11) given in Tables 2 and 3 with parameter values in Table 5, for $G_M = 0.39$ Nm^3/s, $d_p = 1$ mm, $\rho_s = 950$ kg/m^3 (colors indicate axial velocity values). (c) Radial profile of axial velocity along $z = 0.12$ m line in $\theta = 20°$ plane: (-●-) particle-free flow calculated by solving the set of Eqs. (2.1)–(2.2), (2.4)–(2.6) in Table 2, for $G_M = 0.39$ Nm^3/s and (—) particulate flow, calculated by solving the set of Eqs. (2.1)–(3.11) in Tables 2 and 3 with parameter values in Table 5, for $G_M = 0.39$ Nm^3/s, $d_p = 1$ mm, $\rho_s = 950$ kg/m^3. Bed mass = 2 kg.

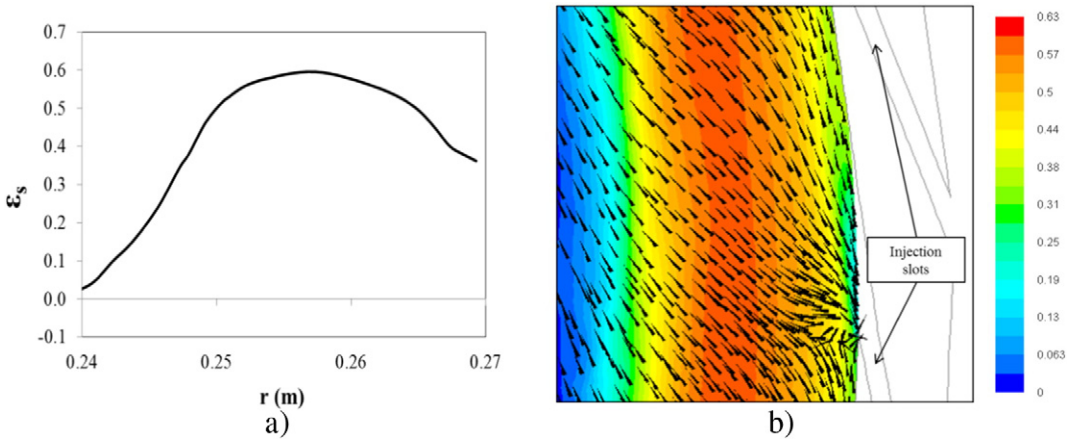

Fig. 5. (a) Radial profile of solids volume fraction along z = 0.05 m line in θ = 20° plane and (b) gas velocity vector field in z = 0.05 m plane superimposed on contour of solids volume fractions for particulate flow calculated by solving Eqs. (2.1)–(3.11) in Tables 2 and 3 with parameter values in Table 5, for $G_M = 0.39\ Nm^3/s$, $d_p = 1\ mm$, $\rho_s = 950\ kg/m^3$. Bed mass = 2 kg.

radial nor azimuthal, the slip velocity will first be analyzed in the respective components.

To estimate the slip velocities, the profiles of the azimuthal and radial velocity of each phase along the radial coordinate are shown in Fig. 6(a) and (b) respectively. In Fig. 6(a), it can be seen that near the circumferential wall (0.26 < r < 0.27 m) where the gas injection slots are located, the gas azimuthal velocity is higher than the solids azimuthal velocity. This is the region where the injected gas transfers most of its momentum to the particles. The entire azimuthal momentum transfer is seen to be transferred over this initial 40% of the bed height starting from the circumferential wall. Beyond this radial position (r < 0.26 m), the azimuthal velocity of both gas phase and solid phase are equal, indicating that the azimuthal slip velocity falls off to zero. Fig. 6(b) shows that in radial direction the solids have zero velocity, as the rotating particles lack any overall radial motion in a stable bed operation. The radial slip velocity thus equals the radial gas velocity. The overall slip velocity is calculated from its radial and azimuthal component as:

$$U_{slip} = \sqrt{U_{\theta,slip}^2 + U_{r,\mathrm{slip}}^2} \tag{2}$$

The change in the main flow features of the GSVU particulate flow, discussed in this section, namely i) pressure drop over the solids bed, ii) solids velocity iii) bed solids volume fraction and iv) slip velocity will next be studied for varying gas flow rate, solids density and particle diameter. The study is performed for a bed with mass of 2 kg for all simulation cases.

3.3. Effect of gas flow rate on GSVU hydrodynamics

Contrary to gravitational fluidized beds, a constant mass fluidized bed in the GSVU, as in the present study, will remain stable with increasing gas flow rate [31]. To investigate this claim, the gas flow rate is extended over a wide range (Table 6, cases 1–6) while particle diameter, solids density and bed mass (2 kg) are kept constant. The range of gas flow rates (cases 1–6, Table 6) is selected such that a stable dense rotating solids bed is established while ensuring a low energy cost for sending pressurized gas through the GSVU in large quantities. The effect on the flow features described in the previous section is studied.

Fig. 7(a) shows an almost proportional increase of the pressure drop over the GSVU bed with increasing gas flow rate. Assuming the radial gas velocity gradients not to be significant and the viscosity of the gas being low, the gas momentum balance (Table 2, Eq. 2.2) over the radial coordinate can be simplified to:

$$\int_{P_0}^{P_i} dP = \int_{r_0}^{r_i} \left(\frac{1}{\varepsilon_g}\beta U_{slip}\right) dr \tag{3a}$$

with r_0 and r_i being the outer radius (circumferential wall) and inner radius (freeboard) of the bed respectively. The equation suggests that the radial pressure drop over the bed is a function of the radial drag force per unit volume acting on the particles. The cumulative drag force acting

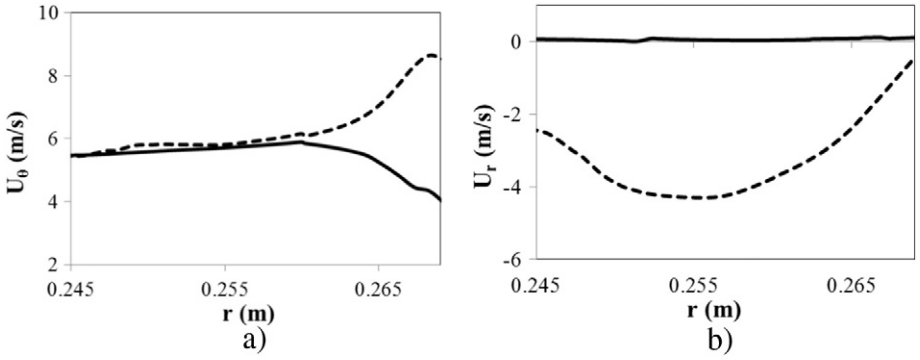

Fig. 6. Radial profiles of (a) azimuthal velocity and (b) radial velocity along z = 0.05 m line in θ = 20° plane: full line, solids and (–) gas, for particulate flow calculated by solving Eqs. (2.1)–(3.11) in Tables 2 and 3 with parameter values in Table 5, for $G_M = 0.39\ Nm^3/s$, $d_p = 1\ mm$, $\rho_s = 950\ kg/m^3$. Bed mass = 2 kg.

on the particles can be expressed as:

$$F_d = \int_{r_0}^{r_i} (2\pi r L)\beta U_{slip} dr \tag{3b}$$

Eqs. (3a)–(3b) indicate that an increase of the drag force on the particles results in an increase in the pressure drop over the bed. When increasing the gas flow through a gravitationally fluidized bed, the increasing drag force on the particles will eventually result in entrainment of the particles, as the gravitational force on the particles remains unaffected. In the GSVU however, the centrifugal force on the particles increases with increasing gas flow rate as more azimuthal momentum is transferred to an invariant number of particles (constant bed mass). Consequently, the particles rotate with a higher azimuthal velocity as seen in Fig. 7(b). The proportional increase in azimuthal solids velocity with increasing gas flow rate has also been experimentally observed by De Wilde and de Broqueville [11]. With increasing azimuthal solids velocity the cumulative centrifugal force acting on the particles also increases in magnitude:

$$F_c = \int_{r_0}^{r_i} (2\pi r L)\rho_s \varepsilon_s \frac{U_{\theta,s}{}^2}{r} dr \tag{4}$$

Therefore, in a GSVU, both the drag force and centrifugal force are altered with changing gas flow rate. Bed stability and particle entrainment for given operating conditions depend on the variation in the ratio of the two forces. It must be highlighted here that the densification of the bed in the GSVU is different from the fluidization behavior observed in a RFB. In a RFB, layer-by-layer fluidization is reported with increasing gas flow rate in RFBs [22,52].

From Fig. 7(c) the centrifugal to radial drag force ratio is seen to increase with increasing gas flow rate. As the ratio remains higher than one the particles will not be entrained and a stable solids bed is maintained for all gas flow rates investigated. With increasing gas flow rate, both the drag force and the centrifugal force increase. The increase in centrifugal force thus overcompensates the increase in radial drag force. Hence, the particles are pushed more strongly towards the circumferential wall and the bed is expected to become more compact. Fig. 7(d) shows that the bed-averaged solids volume fraction initially increases with increasing gas flow rate, making the bed more compact, in agreement with previous experimental studies [11]. Once the maximum packing limit is reached, the solids volume fraction remains nearly constant with increasing gas flow rate. Remark that the solids volume fraction presented in Fig. 7(d) is a bed-averaged value. Although in the middle part of the bed the solids volume fractions approach the maximum packing limit, the dilution of the bed towards the circumferential wall and towards the freeboard (Fig. 5(a)) reduces the bed-averaged solids volume fraction.

From Fig. 8(a)–(c) it is found that with increasing gas flow rate, the azimuthal, radial and total slip velocity increase. In azimuthal direction, the slip velocity varies in a small part of the bed ($0.263 < r < 0.27$ m) only. In the remaining part of the bed, the gas and solids azimuthal velocity are equal and the azimuthal slip velocity drops to zero (Fig. 6(a)). It is also observed that the radius where the azimuthal slip velocity drops to zero decreases with higher gas flow rates. In the radial direction however the interstitial gas velocity increases with increasing gas flow rate while the radial solids velocity is zero at all stable bed conditions (Fig. 6(b)). The increase in slip velocity with increasing gas flow rate, highlights one of the major strengths of the GSVU for process intensification. Increased slip velocities result in improved heat and mass transfer between the phases, without particle entrainment or bed dilution as observed in gravitational fluidized beds.

3.4. Effect of solids properties on GSVU bed hydrodynamics

The effect of solids properties on the GSVU bed hydrodynamics is studied under constant gas flow rate (0.39 Nm^3/s) and constant total bed mas (2 kg). As the centrifugal force acting on the particles is a function of both particle diameter and solids density, while the drag force is primarily but not uniquely influenced by the particle diameter but

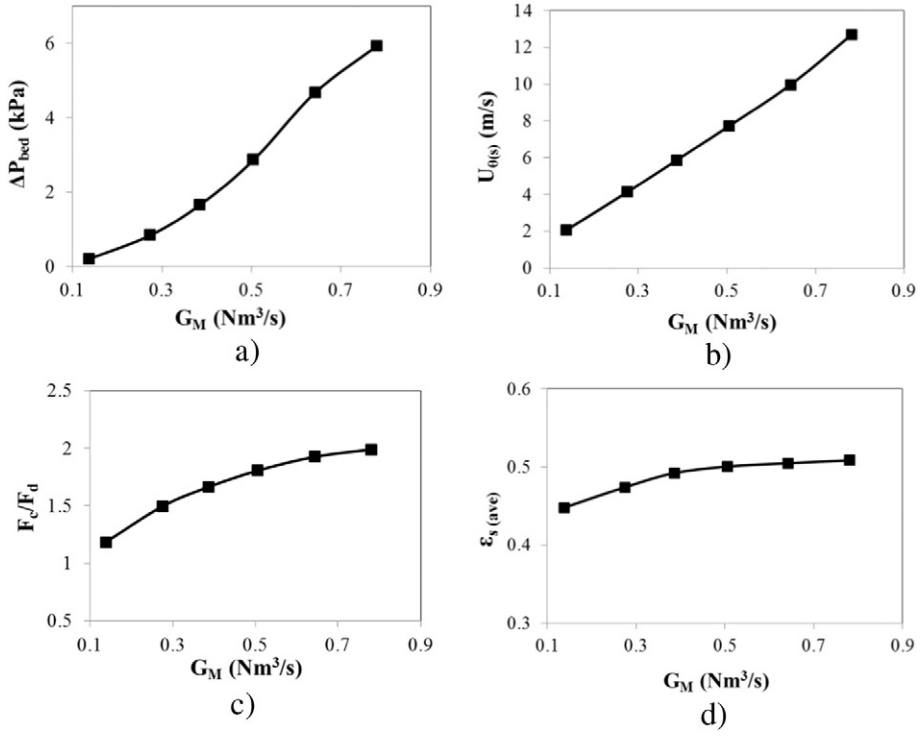

Fig. 7. (a) Bed pressure drop; (b) bed-averaged azimuthal solids velocity; (c) cumulative centrifugal force to radial drag force ratio and (d) bed-averaged solids volume fraction as a function of gas flow rate for particulate flow calculated by solving Eqs. (2.1)–(3.11) in Tables 2 and 3 with parameter values in Table 5, for $d_p = 1$ mm, $\rho_s = 950$ kg/m^3. Bed mass = 2 kg.

hardly by the solids density, both are varied independently in the present study.

3.4.1. Variation in solids density

A study with three solids densities is performed as shown in Table 6 (cases 7–9). The solids densities are representative of biomass (450 kg/m^3), high density polyethylene (HDPE) (950 kg/m^3) and polyvinyl difluoride (PVDF) (1800 kg/m^3). The latter two have been used in previous experimental studies [32] on the effect of solids properties on GSVU bed hydrodynamics. As one of the currently investigated applications for the GSVU technology is fast biomass pyrolysis, a material density representative of the bulk density of biomass is also considered for analysis [28]. The particle diameter is kept constant at 1 mm.

In order to analyze the effect of solids density on the GSVU bed hydrodynamics, the changes in the drag force exerted by the gas on the particles in the solids bed need to be understood. The overall cumulative radial drag force exerted on the solids bed is primarily influenced by the total area available for momentum transfer between the phases. This transfer surface area A_T is calculated as

$$A_T = \left(\frac{A_P}{V_P}\right) V_T \tag{5}$$

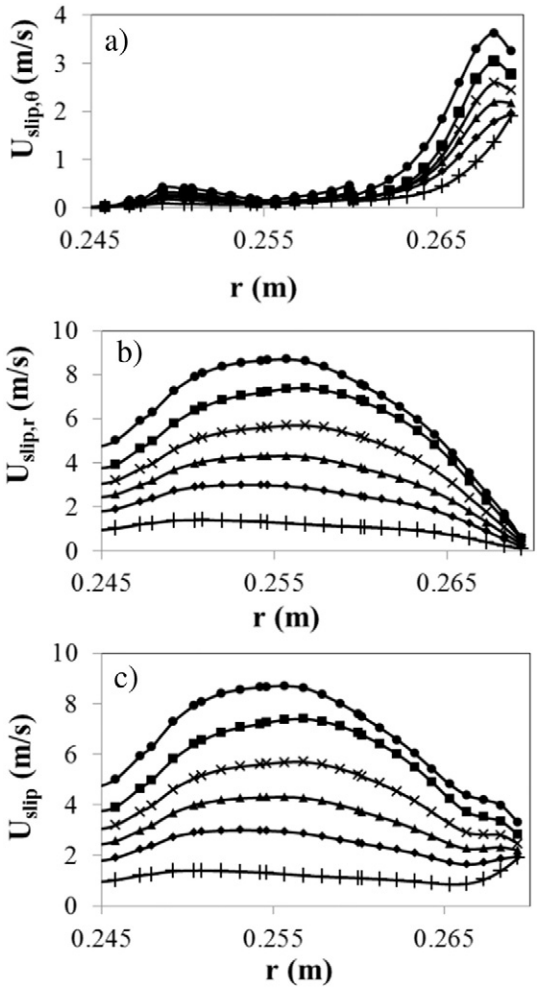

Fig. 8. Radial profiles of (a) azimuthal; (b) radial and (c) total slip velocity obtained along z = 0.05 m line in θ = 20° plane, calculated by solving Eqs. (2.1)–(3.11) in Tables 2 and 3 with parameter values in Table 5, for (-+-) G_M = 0.14 Nm^3/s; (-♦-) G_M = 0.28 Nm^3/s; (-▲-) G_M = 0.39 Nm^3/s; (-×-) G_M = 0.5 Nm^3/s; (-■-) G_M = 0.64 Nm^3/s and (-●-) G_M = 0.78 Nm^3/s, d_p = 1 mm, ρ_s = 950 kg/m^3. Bed mass = 2 kg.

with $\left(\frac{A_P}{V_P}\right)$ being the volumetric cross-sectional area for momentum transfer per particle and V_T the total volume of particles in the bed. For spherical monodisperse particles the specific cross-sectional area per particle is calculated as:

$$\left(\frac{A_P}{V_P}\right) = \frac{3}{2}\frac{1}{d_p} \tag{6}$$

with d_p the particle diameter. In the solids density case study, the particle diameter is kept constant, thus the volumetric cross-sectional area per particle remains unchanged. Lowering the solids density implies that more particles are needed to keep the bed mass at 2 kg. Thus the total volume of particles V_T in the bed increases with decreasing solids density. This can be clearly seen in Fig. 9, which shows the calculated contours of solids volume fraction in the θ = 20° plane for different density materials and a bed mass of 2 kg. With increasing number of particle layers, the total available surface area (A_T) for momentum transfer (Eq. (5)) increases, which will cause the net drag force on the bed to increase.

Indeed from the static gauge pressure profile along the radial coordinate, shown in Fig. 10(a), the pressure drop over the bed is seen to increase with decreasing solids density. As already discussed (Eqs. (3a)–(3b)), an increased pressure drop over the bed corresponds to an increase in the net drag force experienced by the particles. In Fig. 10(b) the azimuthal solids velocity in the θ = 20° plane is seen to increase with decreasing solids density. This seems controversial at first glance. The gas flow rate remaining constant, a constant amount of azimuthal momentum is fed to the GSVU by the gas phase while the total bed mass in the unit is kept constant. Therefore, the velocity of the particles is not expected to vary with solids density. The trend can be explained however by considering the change in the ratio of centrifugal force to radial drag force for different densities, shown in Fig. 11(a). A first observation is that, as the ratio is >1, the bed is pushed towards the circumferential wall due to an unbalanced radially outward force. This results in a wall-normal force pushing the particles against the wall, generating particle-wall friction and hence, slowing down the particles. As the ratio of centrifugal to radial drag force decreases with decreasing solids density, the unbalanced force exerted on the circumferential wall diminishes, resulting in a reduction in particle-wall friction for decreasing solids density. The reduced frictional force on the low density particles will allow them to rotate with higher velocities, as observed in Fig. 10(b). Following this line of argument, the particles should have slowed down with increasing gas flow rate, which was not observed in the previous section (Fig. 7(b)). An increase in the gas flow rate increases the centrifugal to radial drag force ratio, thereby increasing the particle-wall friction. However, the net azimuthal momentum transferred to the particles from the gas phase also increases with increasing gas flow rate. This increase compensates the losses due to particle-wall friction. In the solids density case study the gas flow rate is kept constant and hence, there is no compensation.

The bed-averaged solids volume fractions only slightly decrease with decreasing solids density as can be seen in Fig. 9. Although the bed height increases and the solids volume fraction distribution becomes slightly non-uniform with decreasing solids density, the dense nature of the bed is retained and no macroscopic non-homogeneities such as bubble formation are observed. This can be explained by decreasing centrifugal to radial drag force ratio over the bed (Fig. 11(a)). As the cumulative centrifugal to radial drag force ratio over the entire bed decreases with decreasing solids density, the bed shows a higher degree of radial fluidization resulting in a decrease in the bed-averaged solids volume fractions. Nonetheless, for different solids densities the solids bed is sufficiently dense and stable without particle entrainment or bubble formation, demonstrating the capability of the GSVU to handle a wide range of density in materials.

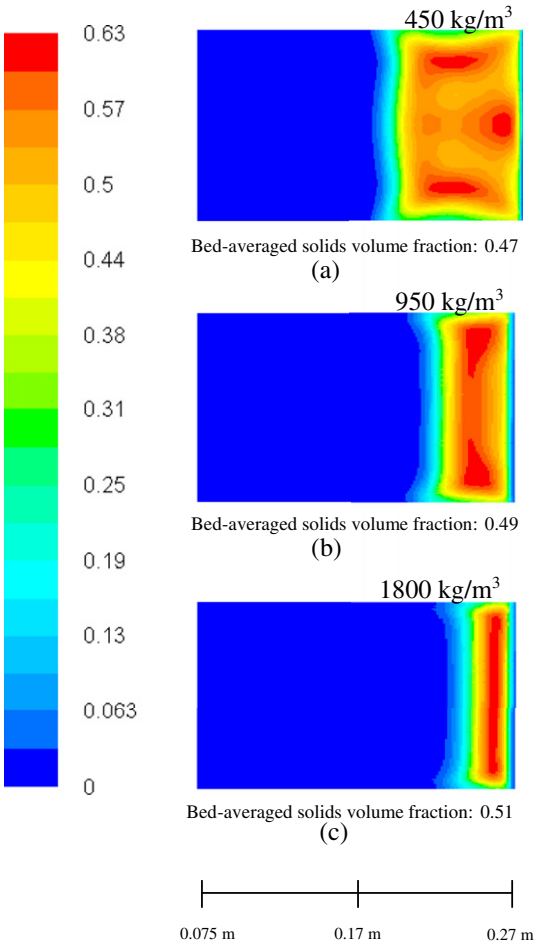

Fig. 9. Contours of solids volume fraction in $\theta = 20°$ plane for different solids densities for particulate flow calculated by solving the set of Eqs. (2.1)–(3.11) given in Tables 2 and 3 with parameter values in Table 5, for $G_M = 0.39\ Nm^3/s$, $d_p = 1$ mm, (a) 450 kg/m^3; (b) 950 kg/m^3 and (c) 1800 kg/m^3. Bed mass = 2 kg.

In Fig. 11(b) the average slip velocity is seen to decrease with decreasing solids density. Since the gas flow rate is kept constant at 0.39 Nm^3/s, the fed radial and azimuthal gas momentum is constant for all beds. Furthermore, the change in the solids volume fractions inside the bed is not significantly altered (Fig. 9). Hence, the radial slip velocity remains mostly unaffected by a change in solids density, as confirmed by the simulations (not shown). However, with decreasing density, the bed rotates faster (Fig. 10(b)) and the azimuthal slip velocity between the gas and the particles diminishes (not shown). This causes a net decrease in the total slip velocity with decreasing solids density (Fig. 11(b)).

3.4.2. Variation in particle diameter

A study with three particle diameters is performed as shown in Table 6 (cases 10–12). The solids density is set at 950 kg/m^3. The particle diameters chosen are 2, 1 and 0.5 mm. The 2 mm and 1 mm particle sizes constitute the size of polymeric materials experimentally investigated. As solids (in form of soft biomass pellets for future reactive flow applications such as fast biomass pyrolysis [28]) will become smaller in diameter due to breakage, a smaller particle diameter (0.05 mm) case has been considered. Remark that, for even smaller sized particles, additional van Der Waals' forces may be generated in between them. Since this force has not been accounted for in the present study, the lower range of the particle diameter is kept limited to 0.05 m.

In Fig. 12(a), the static gauge pressure drop along the radial coordinate in the $\theta = 20°$ plane is seen to increase with decreasing particle diameter, indicating an increase in the overall drag force over the bed (Eqs. (3a)–(3b)). Accounting for the drag model proposed by Gidaspow [53] (Table 3, Eq. 3.4), the local drag force on the particles in the solids bed is an inverse function of the particle diameter. With decreasing particle diameter the number of particles required to keep the bed mass at 2 kg increases (as for decreasing solids density). However, since the particle diameter decreases the total bed volume hardly changes (V_T), as seen in Fig. 13. Moreover, reducing the particle diameter from 2 to 1 mm does not affect the uniformity of the dense bed significantly. Although the solids volume fractions near the central region of the bed decrease slightly with decreasing particle diameter, no macroscopic non-uniformities such as bubble formation are observed. The volume fractions in almost the entire bed reach nearly as high as the maximum packing limit. Reducing the particle diameter from 1 to 0.5 mm however, induces non-uniformity in the solids bed. The decrease in particle diameter to 0.5 mm causes a shift from a uniformly dense solids bed to a bubbling fluidized bed. The appearance of bubbles in the GSVU solids bed with decrease in particle diameter has previously been also observed in experiments [10], thus validating the qualitative trend in the bed behavior observed in the numerical simulations.

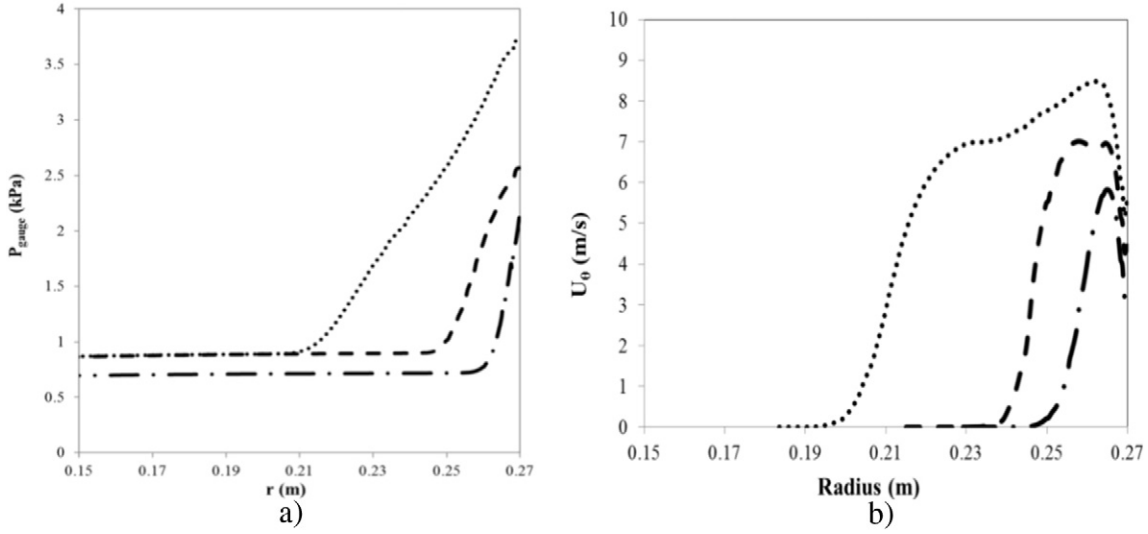

Fig. 10. Radial profiles of (a) static gauge pressure and (b) solids azimuthal velocity obtained along $z = 0.05$ m line in $\theta = 20°$ plane, calculated by solving Eqs. (2.1)–(3.11) in Tables 2 and 3 with parameter values in Table 5, for $G_M = 0.39\ Nm^3/s$, $d_p = 1$ mm, (●●●) $\rho_s = 450$ kg/m^3; (–) $\rho_s = 950$ kg/m^3 and (-●-) $\rho_s = 1800$ kg/m^3. Bed mass = 2 kg.

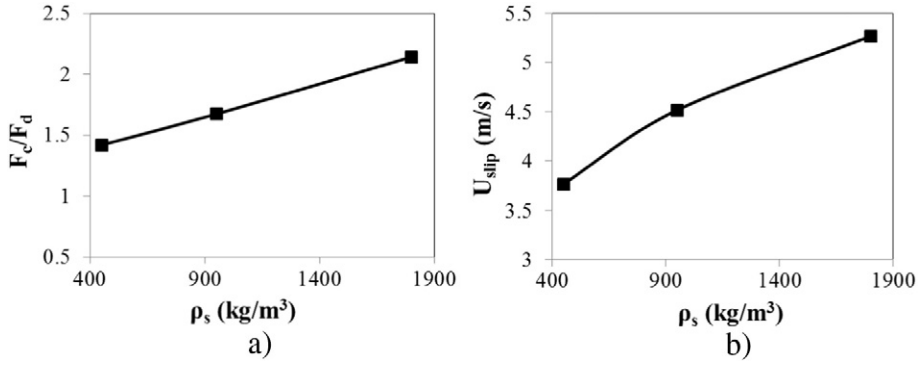

Fig. 11. (a) Cumulative centrifugal force to radial drag force ratio and (b) bed-averaged slip velocity as a function of solids density for particulate flow calculated by solving Eqs. (2.1)–(3.11) in Tables 2 and 3 with parameter values in Table 5, for $G_M = 0.39$ Nm^3/s, $d_p = 1$ mm. Bed mass = 2 kg.

Bubble formation in the bed can be explained by investigating the variation in drag force with decreasing particle diameter. As discussed in the previous section, the drag force acting on the bed is a function of the total surface area A_T for momentum transfer between the phases (Eq. (5)). From Fig. 13, it is already seen that the total solids volume V_T is not significantly affected by a change in particle diameter. The volumetric cross-sectional area $(\frac{A_p}{V_p})$ per particle however, being inversely related to d_p for spherical particles (Eq. (6)), increases with decreasing particle diameter. Thus the drag force acting on a particle increases with decreasing diameter. The centrifugal force acting on a particle however decreases due to the smaller diameter and hence mass, for constant density, of the particles. This local change in the centrifugal to radial drag force ratio, affects the balance over the entire bed. The calculated force ratio over the bed significantly decreases with decreasing particle diameter as shown in Fig. 14. The gas entering through the injection slots forces its way through the particles to form bubbles. For smaller particles (more drag, less apparent weight), gas bubbles will more easily be formed in the bed. This causes a shift to bubbling fluidization as observed in Fig. 13.

In Fig. 12(b), showing the profiles of the azimuthal solids velocity along the radial coordinate for different particle diameters, it is seen that for smaller particles the solids rotate with a higher azimuthal velocity. The reduced centrifugal to radial drag force ratio over the bed for smaller particles (Fig. 14) results in a reduction of the wall-normal force and causes the particles to accelerate as discussed above.

Fig. 12(c) shows the radial profile of the solids volume fraction for different particle diameters. Bubble formation in the bed of 0.5 mm particles causes the bed to expand and become more diluted as gas bubbles entrain small particles in their wake when travelling from the circumferential wall towards the freeboard region of the bed. As the gas passes through the bed in the form of bubbles, the gas-solid contacting area is diminished. Furthermore, bubbles induce radial solids recirculation in

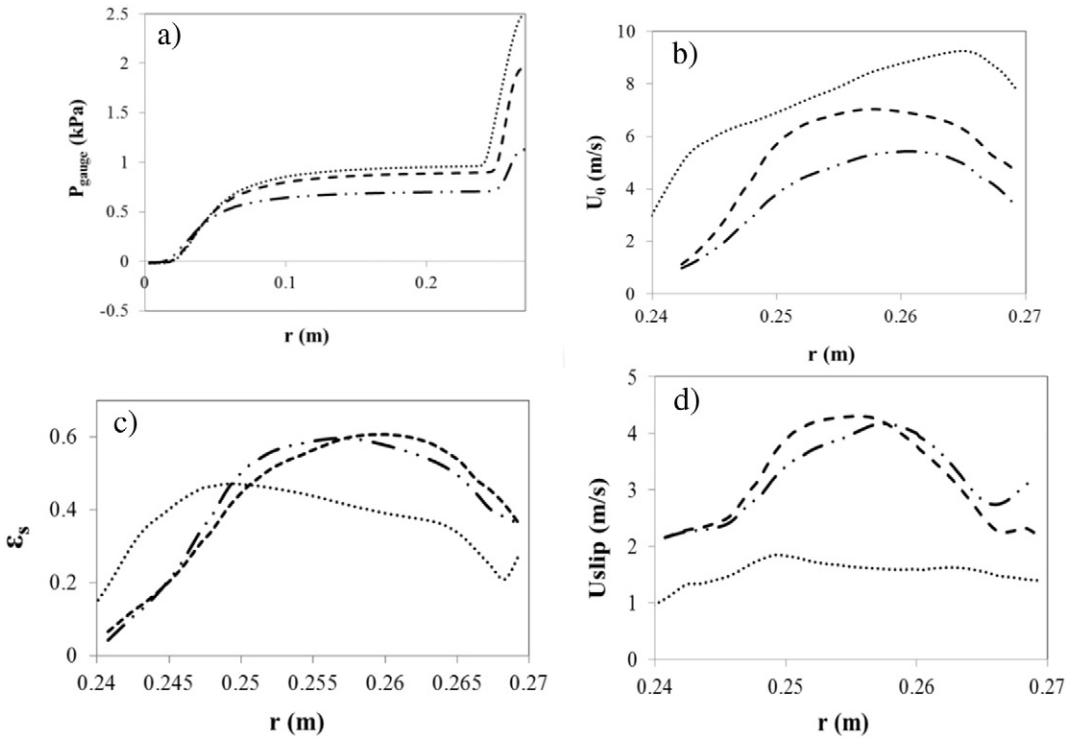

Fig. 12. Radial profiles of (a) static gauge pressure, (b) azimuthal solids velocity, (c) solids volume fraction and (d) slip velocity obtained along z = 0.05 m line in θ = 20° plane, calculated by solving Eqs. (2.1)–(3.11) in Tables 2 and 3 with parameter values in Table 5, for $G_M = 0.39$ Nm^3/s, (●●●) $d_p = 0.5$ mm; (–) $d_p = 1$ mm and (-●●-) $d_p = 2$ mm, $\rho_s = 950$ kg/m^3. Bed mass = 2 kg.

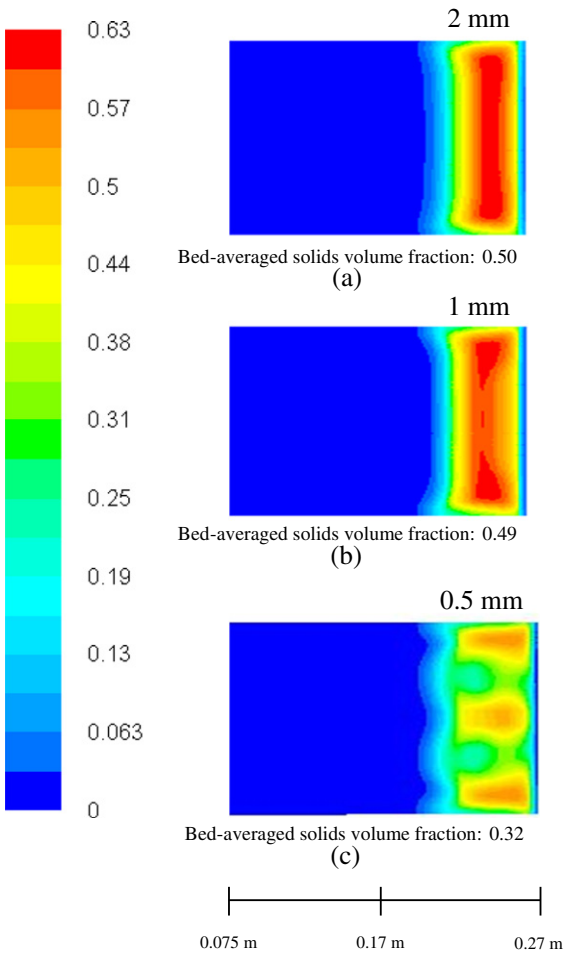

Fig. 13. Contours of solids volume fraction in θ = 20° plane for different particle diameters for particulate flow calculated by solving the set of Eqs. (2.1)–(3.11) given in Tables 2 and 3 with parameter values in Table 5, for $G_M = 0.39\ Nm^3/s$, (a) 2 mm; (b) 1 mm and (c) 0.5 mm, $\rho_s = 950\ kg/m^3$. Bed mass = 2 kg.

the bed. The corresponding reduction in radial velocity significantly reduces the total slip velocity in the bed as seen in Fig. 12(d). A reduction in the total slip velocity will result in a decrease of the heat and mass transfer efficiency of the GSVU. Thus, the bubbling fluidization regime

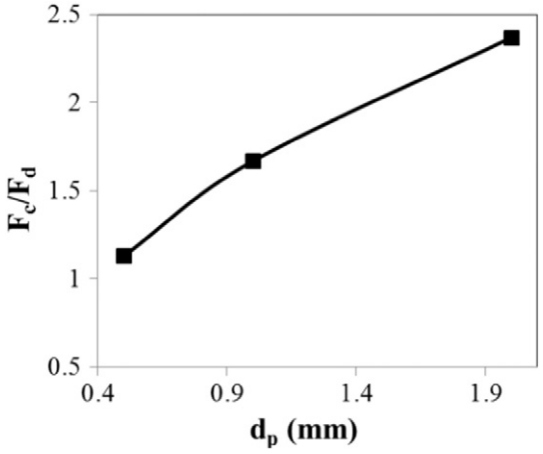

Fig. 14. Cumulative centrifugal force to radial drag force ratio as a function of particle diameter for particulate flow from calculated by solving Eqs. (2.1)–(3.11) in Tables 2 and 3 with parameter values in Table 5, for $G_M = 0.39\ Nm^3/s$, $\rho_s = 950\ kg/m^3$. Bed mass = 2 kg.

is counterproductive for PI. Remark that the present study is performed in an imposed GSVU geometry. The minimum gas flow rate at which bubbling fluidization shifts to uniformly dense bed, for different particle diameters needs further study.

4. Conclusions

This paper explains the gas-solid bed hydrodynamics developing in a Gas-Solid Vortex Unit. To this end, a 3D Eulerian two-phase numerical study using FLUENT v.14a® of a 40° section of a GSVU unit is performed to obtain a proper visualization of the fluidization behavior.

Simulated radial profiles of static gauge pressure and solids velocity are compared with experimental data obtained in a GSVU. The model is found to predict well the pressure drop and solids velocity over a wide range of operating conditions. The validated model is then used for a study of the GSVU fluidization behavior for a range of operating conditions. Flow variables such as the bed pressure drop, solids volume fraction, solids velocity and slip velocity are calculated and analyzed. The simulations indicate that a stable uniformly dense bed can be formed inside the unit at high gas flow rates over a wide range of gas flow rates, solids densities and particle diameters, establishing the GSVU to be suitable for process intensification.

During the case study, no particle entrainment is observed, elaborating the flexibility of operation of the GSVU. With increasing gas flow rate, for constant solids density, particle diameter and bed mass, the increasing centrifugal to radial drag force ratio results in higher solids velocities, more compact beds and higher slip velocities. Contrary to Rotating Fluidized Beds, no radial layer-by-layer fluidization is observed in the GSVU as both azimuthal and radial momentum input of the gas increase simultaneously with increasing gas flow rate. Decreasing the solids density, for constant gas flow rate, particle diameter and bed mass, results in higher solids velocities due to a decrease of friction between the particles and the circumferential wall of the GSVU. At the same time, slip velocity is seen to decrease as the azimuthal solids velocity increases while the gas flow rate remains constant. Decreasing the particle diameter for constant gas flow rate, solids density and bed mass, eventually causes a shift in the fluidization regime and the GSVU bed exhibits bubbling behavior, due to the local reduction of centrifugal to radial drag force ratio. Meanwhile, the slip velocity is seen to decrease due to gas bypassing suggesting a possible decrease in heat and mass transfer efficiency in the GSVU. The model predicts changes in fluidization regime and can thus be used for further studying the fluidization regime maps for the GSVU at different operating conditions and for different types of materials.

Acknowledgments

This work was supported by the European Research Council FP7/2007-2013/ERC grant agreement n° 290793. We are grateful for the use of the Stevin Supercomputer Infrastructure at Ghent University, funded by Ghent University, the Hercules Foundation, and the Flemish Government — department EWI.

References

[1] A.S. Jensen, Pressurized drying in a fluid bed with steam, Proceedings of the Eighth International Drying, Symposium Montreal 1992, pp. 1593–1601.
[2] D.A. Avery, D.H. Tracey, Application of fluidized beds of activated carbon in solvent recovery from air or gas streams, Tripartite Chemical Engineering Conference Montreal 1968, pp. 28–33.
[3] S.J. Maronga, P. Wnukowski, The use of humidity and temperature profiles in optimizing the size of fluidized bed in a coating process, Chem. Eng. Process. Process Intensif. 37 (1998) 423–432.
[4] H. Nakaishi, Chemical Reactors Baifukan, 1984 177.
[5] F.J. Karol, Studies with high activity catalysts for olefin polymerization, Catal. Rev. 26 (1984) 557–595.
[6] G. Froment, K.B. Bischoff, J. DeWilde, Chemical Reactor Analysis and Design, third ed. John Wiley & Sons, Inc., 2010

[7] A. Ahmadzadeh, H. Arastoopour, Three-dimensional numerical simulation of a horizontal rotating fluidized bed, Powder Technol. 183 (2008) 410–416.
[8] W. Zhang, A review of techniques for the process intensification of fluidized bed reactors, Chin. J. Chem. Eng. 17 (2009) 688–702.
[9] A. Ahmadzadeh, H. Arastoopour, F. Teymoour, Rotating fluidized bed an efficient polymerization reactor, AIChE Annual Meeting Cincinnati, 2005 (Ohio).
[10] J. De Wilde, A. de Broqueville, Rotating fluidized beds in a static geometry: experimental proof of concept, AICHE J. 53 (2007) 793–810.
[11] J. De Wilde, A. de Broqueville, Experimental study of fluidization of 1G-Geldart D-type particles in a rotating fluidized bed with a rotating chimney, AICHE J. 54 (2008) 2029–2044.
[12] E.P. Volchkov, N.A. Dvornikov, A.N. Yadykin, Characteristic Features of Heat and Mass Transfer in a Fluidized Bed in a Vortex Chamber, 34, 2003 13.
[13] D.G. Kroger, G. Abdelnour, E.K. Levy, J.C. Chen, Centrifugal fluidization: effects of particle density and size distribution, Chem. Eng. Commun. 5 (1980) 55–67.
[14] G.-H. Qian, I. Bágyi, I.W. Burdick, R. Pfeffer, H. Shaw, J.G. Stevens, Gas–solid fluidization in a centrifugal field, AICHE J. 47 (2001) 1022–1034.
[15] S. Matsuda, H. Hatano, T. Muramoto, A. Tsutsumi, Modeling for size reduction of agglomerates in nanoparticle fluidization, AICHE J. 50 (2004) 2763–2771.
[16] P. Eliaers, A. de Broqueville, A. Poortinga, T. van Hengstum, J. De Wilde, High-G, low-temperature coating of cohesive particles in a vortex chamber, Powder Technol. 258 (2014) 242–251.
[17] L.T. Fan, C.C. Chang, Y.S. Yu, T. Takahashi, Z. Tanaka, Incipient fluidization condition for a centrifugal fluidized bed, AICHE J. 31 (1985) 999–1009.
[18] H. Nakamura, T. Iwasaki, S. Watano, Experimental analysis of bubble velocity in a rotating fluidized bed, Chem. Eng. Process. Process Intensif. 48 (2009) 178–186.
[19] L.A. Anderson, S.H. Hasinger, B.N. Turman, Two-component vortex flow studies of the colloid core nuclear rocket, J. Spacecr. Rocket. 9 (1972) 311–317.
[20] J.J. Smulsky, The Aerodynamics and Process in the Vortex Chamber, Science, Tyumen, Russia, 1992.
[21] R. Ekatpure, G. Heynderickx, A.D. Broqueville, G.B. Marin, Experimental Investigation of Rotating Fluidized Bed in Static Geometry, European Process Intensification Conference 2nd, PresentationsVenice, Italy, 2009.
[22] Y.-M. Chen, Fundamentals of a centrifugal fluidized bed, AICHE J. 33 (1987) 722–728.
[23] A. Dutta, R.P. Ekatpure, G.J. Heynderickx, A. de Broqueville, G.B. Marin, Rotating fluidized bed with a static geometry: guidelines for design and operating conditions, Chem. Eng. Sci. 65 (2010) 1678–1693.
[24] F.A. Bykovskii, S.A. Zhdan, V.V. Mitrofanov, E.F. Vedernikov, Self-ignition and special features of flow in a planar vortex chamber, Combustion, Explosion and Shock Waves, 35, 1999, pp. 622–636.
[25] V.V. Lukashov, A.V. Mostovoi, Investigation of a Vortex Combustion Chamber with a Centrifugal Fluidized Bed, 37, 2006 685–690.
[26] A.S. Timonin, V.I. Mushtaev, Z.T. Nguen, A.A. Pakhomov, A.G. Ryauzov, Spiral-vortex apparatus — effective equipment for the heat treatment of disperse materials, Chem. Pet. Eng. 33 (1997) 7–10.
[27] A.S. Belousov, B.S. Sazhin, Characteristics of flow structures in units for processing fibre-forming polymers inactive hydrodynamic regimes, Fibre Chemistry 39 (2007) 475–479.
[28] R.W. Ashcraft, G.J. Heynderickx, G.B. Marin, Modeling fast biomass pyrolysis in a gas–solid vortex reactor, Chem. Eng. J. 207–208 (2012) 195–208.
[29] R.W. Ashcraft, J. Kovacevic, G.J. Heynderickx, G.B. Marin, Assessment of a gas–solid vortex reactor for SO2/NOx adsorption from flue gas, Ind. Eng. Chem. Res. 52 (2013) 861–875.
[30] V. Shtern, Counterflows: Paradoxical Fluid Mechanics Phenomena, Cambridge University Press, 2012.
[31] J.Z. Kovacevic, M.N. Pantzali, G.J. Heynderickx, G.B. Marin, Bed stability and maximum solids capacity in a gas–solid vortex reactor: experimental study, Chem. Eng. Sci. 106 (2014) 293–303.
[32] J.Z. Kovacevic, M.N. Pantzali, K. Niyogi, N.G. Deen, G.J. Heynderickx, G.B. Marin, Solids velocity fields in a cold-flow gas–solid vortex reactor, Chem. Eng. Sci. 123 (2015) 220–230.
[33] L.M. Kochetov, B.S. Sazhin, E.A. Karlik, Hydrodynamics and heat exchange in vortex drying chambers, Chem. Pet. Eng. 5 (1969) 688–690.
[34] E.P. Volchkov, V.I. Terekhov, A.N. Kaidanik, A.N. Yadykin, Aerodynamics and heat and mass transfer of fluidized particle beds in vortex chambers, Heat Transfer Eng. 14 (1993) 36–47.
[35] J.L. Sinclair, R. Jackson, Gas-particle flow in a vertical pipe with particle-particle interactions, AICHE J. 35 (1989) 1473–1486.
[36] W. Rosales Trujillo, J. De Wilde, Fluid catalytic cracking in a rotating fluidized bed in a static geometry: a CFD analysis accounting for the distribution of the catalyst coke content, Powder Technol. 221 (2012) 36–46.
[37] A. de Broqueville, J. De Wilde, Numerical investigation of gas-solid heat transfer in rotating fluidized beds in a static geometry, Chem. Eng. Sci. 64 (2009) 1232–1248.
[38] J. Baeyens, D. Geldart, An investigation into slugging fluidized beds, Chem. Eng. Sci. 29 (1974) 255–265.
[39] R.P. Ekatpure, V.U. Suryawanshi, G.J. Heynderickx, A. de Broqueville, G.B. Marin, Experimental investigation of a gas–solid rotating bed reactor with static geometry, Chem. Eng. Process. Process Intensif. 50 (2011) 77–84.
[40] M.N. Pantzali, J.Z. Kovacevic, G.J. Heynderickx, G.B. Marin, V.N. Shtern, Radial pressure profiles in a cold-flow gas-solid vortex reactor, AICHE J. 61 (2015) 4114–4125.
[41] T.B. Anderson, R. Jackson, Fluid mechanical description of fluidized beds. Equations of motion, Ind. Eng. Chem. Fundam. 6 (1967) 527–539.
[42] J.T. Jenkins, S.B. Savage, A theory for the rapid flow of identical, smooth, nearly elastic, spherical particles, J. Fluid Mech. 130 (1983) 187–202.
[43] D. Gidaspow, Multiphase Flow and Fluidization: Continuum and Kinetic Theory Descriptions, Academic Press, 1994.
[44] V. Yakhot, S.A. Orszag, Renormalization group analysis of turbulence. I. Basic theory, J. Sci. Comput. 1 (1986) 3–51.
[45] B.E. Launder, D.B. Spalding, The numerical computation of turbulent flows, Comput. Methods Appl. Mech. Eng. 3 (1974) 269–289.
[46] G.H. Vatistas, M. Fayed, J.U. Soroardy, Strongly swirling turbulent sink flow between two stationary disks, J. Propuls. Power 24 (2008) 295–301.
[47] P.A. Moysey, M.R. Thompson, Determining the collision properties of semi-crystalline and amorphous thermoplastics for DEM simulations of solids transport in an extruder, Chem. Eng. Sci. 62 (2007) 3699–3709.
[48] K. Goro, K. Kimitoshi, Restitution coefficient in a collision between two spheres, Jpn. J. Appl. Phys. 26 (1987) 1230.
[49] P.C. Johnson, R. Jackson, Frictional–collisional constitutive relations for granular materials, with application to plane shearing, J. Fluid Mech. 176 (1987) 67–93.
[50] S.V. Patankar, Numerical Heat Transfer and Fluid Flow, McGraw-Hill, New York, 1980.
[51] J. De Wilde, Gas–solid fluidized beds in vortex chambers, Chem. Eng. Process. Process Intensif. 85 (2014) 256–290.
[52] A. Ahmadzadeh, H. Arastoopour, F. Teymour, Numerical simulation of gas and particle flow in a rotating fluidized bed, Ind. Eng. Chem. Res. 42 (2003) 2627–2633.
[53] D. Gidaspow, R. Bezburuah, J. Ding, Hydrodynamics of circulating fluidized beds: kinetic theory approach, Fluidization VII, Proceedings of the 7th Engineering Foundation Conference on Fluidization 1992, pp. 75–82.
[54] C.K.K. Lun, S.B. Savage, D.J. Jeffrey, N. Chepurniy, Kinetic theories for granular flow: inelastic particles in Couette flow and slightly inelastic particles in a general flowfield, J. Fluid Mech. 140 (1984) 223–256.
[55] S. Ogawa, A. Umemura, N. Oshima, On the equations of fully fluidized granular materials, Zeitschrift für angewandte Mathematik und Physik ZAMP, 31 483–493.
[56] M. Syamlal, W. Rogers, T.J. O'Brien, MFIX Documentation Theory Guide, Other Information: PBD: Dec 1993, 1993 (Medium: ED; Size: 49 p).
[57] D.G. Schaeffer, Instability in the evolution equations describing incompressible granular flow, J. Differ. Equ. 66 (1987) 19–50.